Implicit Representation Embraces Challenging Attributes of Pulmonary Airway Tree Structures

Minghui Zhang[1,2], Hanxiao Zhang[1], Xin You[1,2], Guang-Zhong Yang[1], and Yun Gu[1,2(✉)]

[1] Institute of Medical Robotics, Shanghai Jiao Tong University, Shanghai, China
geron762@sjtu.edu.cn
[2] Department of Automation, Shanghai Jiao Tong University, Shanghai, China

Abstract. High-fidelity modeling of the pulmonary airway tree from CT scans is critical to preoperative planning. However, the granularity of CT scan resolutions and the intricate topologies limit the accuracy of manual or deep-learning-based delineation of airway structures, resulting in coarse representation accompanied by spike-like noises and disconnectivity issues. To address these challenges, we introduce a Deep Geometric Correspondence Implicit (DGCI) network that implicitly models airway tree structures in the continuous space rather than discrete voxel grids. DGCI first explores the intrinsic topological features shared within different airway cases on top of implicit neural representation (INR). Specifically, we establish a reversible correspondence flow to constrain the feature space of training shapes. Moreover, implicit geometric regularization is utilized to promote a smooth and high-fidelity representation of fine-scaled airway structures. By transcending voxel-based representation, DGCI acquires topological insights and integrates geometric regularization into INR, generating airway tree structures with state-of-the-art topological fidelity. Detailed evaluation results on the public dataset demonstrated the superiority of the DGCI in the scalable delineation of airways and downstream applications. Source codes can be found at: https://github.com/EndoluminalSurgicalVision-IMR/DGCI.

Keywords: Deep Geometric Correspondence· Implicit Neural Networks · Airway Tree Modeling

1 Introduction

High-fidelity airway tree modeling is critical to preoperative planning, as endobronchial interventions are recognized for their minimally invasive nature in treating pulmonary diseases [12, 19, 22]. Due to the fine-scaled airway structures, manual annotation is error-prone, and highly relied on the expertise of clinicians. The annotation is performed slice-by-slice in image stacks, therefore, the reconstructed shape is inevitably affected by the resolution of discrete voxels. Furthermore, the distinctiveness of the CT images degrades along with the bronchi becoming finer. These attributes result in the coarse delineation of airway tree structures, along with spike-like noise disturbance, as seen in Fig.1.a.1). As

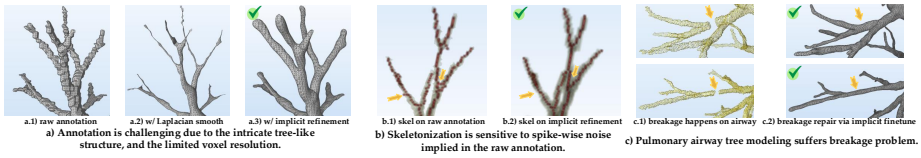

Fig. 1. The challenging attributes of the pulmonary airway tree structures.

demonstrated in Fig.1.a.2), Laplacian smoothing [6] fails to ensure high-fidelity of airways while eliminating the spike-like noise disturbance. In addition, This type of disturbance is detrimental to the skeleton extraction [10] because it is intrinsically sensitive to spike-like noises [1, 3, 26], as revealed in Fig.1.b.1). ith the advancement of convolutional neural networks (CNN), automatic airway tree modeling methods [2,7,9,13,18,24,27,28] were developed to reduce the burden of manual delineation. However, they still model the airway structure in the discrete voxel space, thereby encountering the aforementioned issues as well. CNN-based methods can be trained using preoperatively annotated data for inference on intraoperative data within the same patient, relieving the burden of repetitive labeling. However, in this scenario, the breakage problem is prone to occur [25], leading to the interrupted trajectory in the navigation. The discontinuity disturbs automatic preoperative path planning algorithms, leading to interrupted trajectories and wrong results for radiologists.

To address these challenges, we propose to utilize the implicit neural representation (INR) to embrace these challenging attributes. INRs [5, 15–17] employ coordinate-based neural networks to parameterize the shapes in the continuous physical space rather than the discrete voxel grids. They break the limitation of the grid resolution of CT scans for the delineation of airways. Therefore, INR facilitates a smoother annotation with high-fidelity and reduces the incidence of spike-like noises. However, the underlying topological constraints within the same category shape have not been well explored. Specifically, [15–17] mainly focused on implicit surface reconstruction and can not extract topological correspondence within the class. The implicit template and deformation proposed in [5] were jointly optimized but insufficiently constrained. To mitigate this issue, we propose a novel Deep Geometric Correspondence Implicit (DGCI) network to implicitly model airway structures in the continuous space, and simultaneously explore the intrinsic topological features shared within different airway cases to constrain the learned feature space of training shapes. Unlike DeepSDF [16], which focuses solely on implicit surface reconstruction, DGCI addresses underlying topological constraints within the same category. It promotes the learning of the topological airway shape priors, which is beneficial to repair the breakage. We hypothesize that airway structures share topological consistency among different cases, e.g., the continuity, as they are all single-connected tree structures. DGCI first constructs a reversible correspondence flow between the instance space and the shared space. In the instance space, the coordinates along with the instance-specific latent code are first processed by an implicit SDF function,

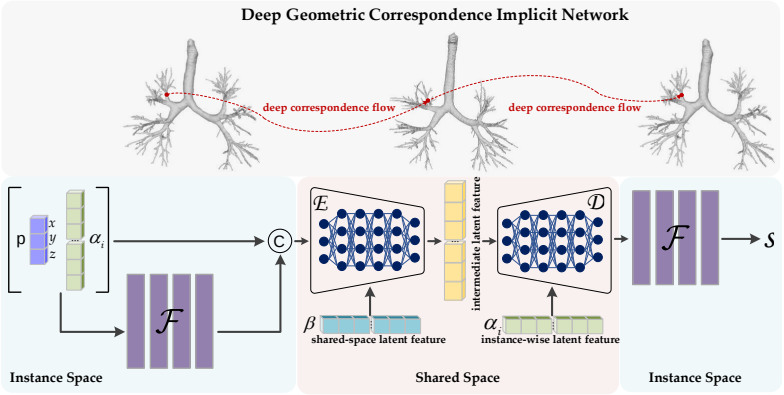

Fig. 2. Framework of the Deep Geometric Correspondence Implicit (DGCI) network.

and then fed into the shared-space implicit encoder to acquire the intermediate latent feature. Then the intermediate latent feature is mapped back to the original physical instance space via the instance-wise implicit decoder, followed by the SDF function to acquire the sdf values. Through this deep correspondence flow, the implicit shape modeling of airways is regularized by the intrinsic topological constraint. Further, inspired by [8], implicit geometric regularization is adopted in DGCI to encourage the unit norm gradients of implicit SDF function to reach good local minima, favoring smooth surface reconstruction without sacrificing fidelity. Our proposed DGCI network generates airway tree structures with state-of-the-art topological fidelity and smoothness, as seen in Fig.1.a.3). The DGCI network not only ensures the scalable delineation of airways but also benefits the downstream applications (skeletonization and breakage repair). The improved smoothness reduces the spike-wise noise, hence, enhances the accuracy of the skeletonization, as depicted in Fig.1.b.2). As for the breakage repair, an effective implicit fine-tune framework is proposed to repair the breakage given the learned shape prior by the DGCI, seen in Fig.1.c.2). Compared with other state-of-the-art methods, our method revealed the superiority in both scalable delineation of airways with high fidelity and downstream applications.

2 Method

2.1 Deep Geometric Correspondence Implicit Network

Inspired by DeepSDF [16], we define a neural field function $\mathcal{F}$ to represent the airway structures as the signed distance field (SDF) in the continuous space. $\mathcal{F}$ takes the given physical coordinate $p \in \mathbb{R}^3$, along with the latent code $\alpha_i \in \mathbb{R}^{\mathrm{K}}$ as input, and outputs the SDF value: s, $\mathcal{F}\ (p; \alpha_i) \in \mathbb{R}^{3+\mathrm{K}} \rightarrow s \in \mathbb{R}$. To implicitly model the airway structures in the continuous space, and simultaneously explore the intrinsic topological features shared within cases as constraints for

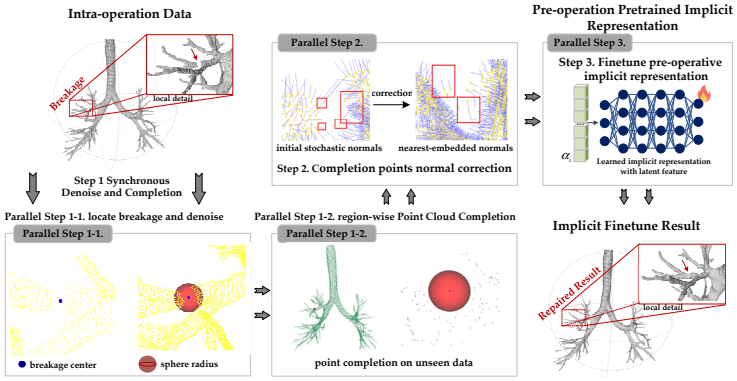

Fig. 3. The implicit fine-tune framework on top of DGCI for airway breakage repair.

the learning process, we propose the Deep Geometric Correspondence Implicit (DGCI) network, illustrated in Fig.2. In general, we perform a reversible deep correspondence flow between the instance space and the shared space, aiming to strengthen the topological constraints shared within instances. The deep correspondence flow is constructed mainly based on an implicit Encoder-Decoder structure, termed DGCI-ED. Both the encoder E and the decoder D are implemented by Multilayer Perceptrons (MLPs). E and D are driven by the instance-wise latent code α_i and shared-space latent code β, respectively. Followed by the design of hypernetwork [4, 21], we use α_i and β to construct separate hypernetworks, ϕ_{α_i}, and ϕ_β, for E and D. The ϕ_{α_i} and ϕ_β also comprise a set of MLPs, each responsible for the weights of a single fully-connected layer i within the E and D. Hence, the DGCI-ED is defined as DGCI-ED $= D_{\phi_{\alpha_i}} \circ E_{\phi_\beta}$. E_{ϕ_β} is driven by the unique latent code ϕ_β shared by all instances, which constrains the shape modeling process to learn intrinsic topological features. Specifically, E_{ϕ_β} takes physical coordinates along with SDF values generated by $\mathcal{F}$ as input and encodes these geometric information into the intermediate latent feature z_i. $\mathcal{F}$ is also implemented based on the hypernetwork that is parameterized by instance-wise latent code α_i. The intermediate feature z_i is defined as:

$$E_{\phi_\beta}(p, \mathcal{F}\ (p; \alpha_i)) = E_{\phi_\beta}(p, \mathcal{F}_{\phi_{\alpha_i}}(p)) \rightarrow z_i \in \mathbb{R}^{\mathrm{K}}. \tag{1}$$

Upon acquiring the intermediate latent feature z_i, the feature correspondence from the instance space to the shared space has been built. Next, to obtain the SDF value of the original shape, $D_{\phi_{\alpha_i}}$ converts the intermediate latent feature back to the instance space, followed by the $\mathcal{F}$ to acquire final SDF values: $\mathcal{F}_{\phi_{\alpha_i}}(D_{\phi_{\alpha_i}}(z_i)) \rightarrow s \in \mathbb{R}$. The overall design of the DGCI is clarified as follows:

$$\mathcal{F}(\text{DGCI-ED}(p; \alpha_i, \beta)) = \mathcal{F}_{\phi_{\alpha_i}}(D_{\phi_{\alpha_i}} \circ E_{\phi_\beta}(p, \mathcal{F}_{\phi_{\alpha_i}}(p))) \rightarrow s \in \mathbb{R}. \tag{2}$$

For simplicity, we use $\mathcal{F}(p; \alpha_i, \beta)$ instead of $\mathcal{F}(\text{DGCI-ED}(p; \alpha_i, \beta))$ to clarify the following optimization process. DeepSDF [16] only constrains the $\mathcal{L}_1$ loss

function between the predicted SDF values and ground-truth SDF values, which is not sufficient to model the fine-scaled airway structure with high fidelity. Inspired by [8], we add additional geometric regularization to facilitate smooth and high-fidelity implicit representation on fine-scaled airway structures. First, the gradients of the implicit function $\mathcal{F}(p;\alpha_i,\beta)$ with regard to surface points are encouraged to be close to the given normals. Second, the Eiknoal term is introduced to force the gradients of $\mathcal{F}(p;\alpha_i,\beta)$ to be of unit 2-norm.

2.2 Optimization Procedure

The main objective function $\mathcal{L}_{sdf}$ that optimizes the $\mathcal{F}(p;\alpha_i,\beta)$ consists of two components, $\mathcal{L}_{sdf} = \mathcal{L}_{sdf-val} + \mathcal{L}_{sdf-geo}$. These two components respectively optimize the values and geometries of the predicted SDF of the shapes:

$$\mathcal{L}_{sdf-val} = \sum_i (\omega_s \sum_{p\in\Omega_i} \left| \mathcal{F}(p;\alpha_i,\beta) - s^{'} \right| + \omega_\varphi \sum_{p\in\Omega_i\setminus S_i} \varphi(\mathcal{F}(p;\alpha_i,\beta))), \tag{3}$$

$$\begin{aligned} \mathcal{L}_{sdf-geo} = \sum_i (\omega_n \sum_{p\in S_i} (1 - \mathrm{S}_{\cos}(\nabla\mathcal{F}(p;\alpha_i,\beta), n^{'})) + \\ \omega_{Eik} \sum_{p\in\Omega_i} |\|\nabla\mathcal{F}(p;\alpha_i,\beta)\|_2 - 1|), \end{aligned} \tag{4}$$

where Ω_i and S_i denote the whole space and the surface of the i^{th} instance, respectively. $s^{'}$ and $n^{'}$ indicate the ground-truth of SDF and surface normal, respectively. Eq.3 directly supervises the SDF regression results and penalizes off-surface points with SDF prediction to zero: $\varphi(s) = \exp(-\delta \cdot \|s\|), \delta \gg 1$. Eq.4 supervises the normal consistency and enforces the amplitude of the SDF gradient function determined by the Eiknonal equation, $\mathrm{S}_{\cos}$ represents cosine similarity measurement. In addition, we employ the intra-regularization and inter-regularization on α_i and β, $\mathcal{L}_{reg} = \mathcal{L}_{intra-reg} + \mathcal{L}_{inter-reg}$: $\mathcal{L}_{intra-reg} = \omega_{intra}(\sum_i \|\alpha_i\|_2^2 + \|\beta\|_2^2), \mathcal{L}_{inter-reg} = \omega_{inter} \sum_i (\|\alpha_i - \beta\|_2^2)$. where the $\mathcal{L}_{intra-reg}$ regularizes instance-space latent codes α_i and β separately, the $\mathcal{L}_{inter-reg}$ ensures the similarity between various instance latent codes and the shared latent code. In addition, we introduce $\mathcal{L}_{cor}$ to ensure the accuracy of the deep correspondence flow: $\mathcal{L}_{cor} = \sum_i (\omega_{cor} \sum_{p\in S_i} (\left\| p - D_{\phi_{\alpha_i}}(z_i) \right\|_2^2))$. In total, the optimization of the DGCI can be summarized as $\mathcal{L}_{total} = \mathcal{L}_{sdf} + \mathcal{L}_{reg} + \mathcal{L}_{cor}$.

2.3 Downstream Applications of DGCI

Skeletonization. Given that the transformation between the image coordinates and the physical coordinates is invertible, we perform the inverse transform to map the reconstructed shape surface via DGCI back to its image coordinate system. Then the hole-filling algorithm is conducted to acquire the dense volume.
Breakage Repair. We propose an effective implicit fine-tune framework for the

Table 1. Quantitative results of the airway shape representation. Results are reported by mean ± standard deviation. TD, BD, Dice are reported in percentage form (%).

Method	Continuous Space			Discrete Space		
	NM-V ↓	NM-E ↓	NM-F ↓	TD ↑	BD ↑	Dice ↑
MC [11]	30.9±20.9	120.1±83.0	2102.4±1094.9	–	–	–
MC w/ Lap	15.0±10.0	450.7±213.7	1656.9±662.6	–	–	–
Occ [15]	4.7±1.7	12.6±9.3	338.3±160.7	28.7±7.6	27.2±7.3	73.5±3.9
Con-Occ [17]	2.1±1.5	20.4±7.2	1309.7±395.4	43.2±11.1	43.6±11.0	75.1±3.75
DeepSDF [16]	1.5±0.9	7.1±6.7	276.5±190.6	82.3±11.9	84.2±11.7	79.8±4.3
DIFNet [5]	0.7±0.3	5.1±4.9	265.9±197.4	89.4±13.4	91.5±12.5	82.5±4.2
DGCINet (ours)	**0.0**±0.0	**4.6**±6.6	**235.3**±170.5	**98.6**±1.4	**99.7**±0.7	**91.2**±2.0

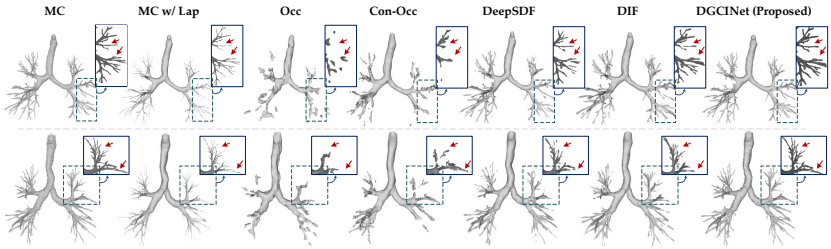

Fig. 4. Visualization of reconstructed airway shapes. The blue boxes and red arrows denote the locally detailed structures magnified for better comparison.

breakage repair, as seen in Fig.3. The point cloud data refinement was first introduced to avoid overfitting local fractured patterns during the fine-tune stage. Specifically, it includes the synchronous point cloud denoising and completion, followed by the correction of normals for the complemented point clouds. Take the single breakage as an example, the breakage generates two isolated connected components, denoted as $\mathcal{X}$ and $\mathcal{Y}$, respectively. The closet point-pair $\{x^*, y^*\}$ is defined as $x^* = \min_{x\in\mathcal{X}}(\min_{y\in\mathcal{Y}} \|x-y\|_2), y^* = \min_{y\in\mathcal{Y}}(\min_{x\in\mathcal{X}} \|y-x\|_2)$. The breakage center is defined as $\frac{1}{2}(x^*+y^*)$, and the breakage radius is $\frac{1}{2}\|x^*-y^*\|_2^2$. The points that lie in the radius range are removed as noises brought by the breakage. Meanwhile, we conducted the point cloud completion based on [23]. The complemented points that lie in the radius range are chosen. Next, the normals of the complemented points are assigned by k-nearest neighbors embedding. Subsequently, the pretrained DGCI takes refined data as input, and fine-tune to repair the breakage based on the learned shape prior. Multiple breakages can be processed as several independent breakages.

3 Experiments and Results

Datasets. The public Binary Airway Segmentation (BAS) dataset [18] contains 90 CT scans with the airway annotation. We split them into 50, 20, and 20

Table 2. Quantitative results about the skeletonization of airways.

Method	CD ↓ (mean ± std)	EMD ↓ (mean ± std)	CD ↓ (median)	EMD ↓ (median)
skel [10]	2.26±2.20	7.54±1.97	1.47	7.40
cldice [20]	2.91±2.60	8.94±2.22	2.24	8.40
gbo-skel [14]	2.48±4.00	8.14±3.94	0.74	6.83
DGCINet + skel	**0.14±2.20**	**4.81±1.97**	**0.11**	**4.61**

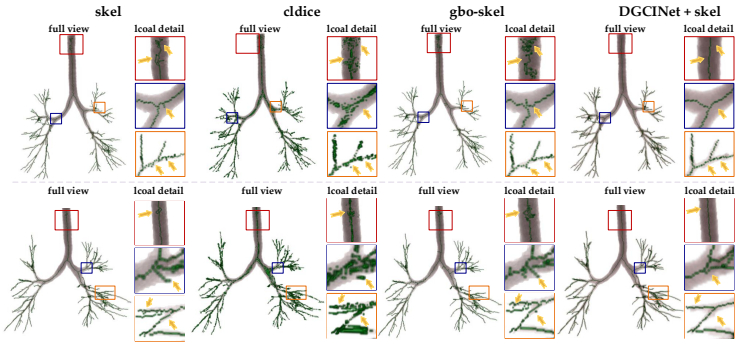

Fig. 5. Visualization of the skeletonization results. The boxes and yellow arrows denote local differences generated by different methods.

instances into training, validation, and testing sets, respectively. As the annotation is provided by the 3D volume, we first obtain the shape surface by Marching Cube, and then follow [16] to prepare the normalized SDF points.

Implementation Details. The E_{ϕ_β} and $D_{\phi_{\alpha_i}}$ were implemented by three and two hidden layers of MLPs, respectively. The SDF function $\mathcal{F}$ was designed by four hidden layers of MLPs. The weights of each single fully connected layer of E_{ϕ_β}, $D_{\phi_{\alpha_i}}$, and $\mathcal{F}$ were decided by three hidden layers of the hypernetwork ϕ. ϕ_{α_i} took instance-specific latent code as input and was responsible for the weights of the $D_{\phi_{\alpha_i}}$ and $\mathcal{F}$. The shared-space latent code β was adopted to drive the E_{ϕ_β}, which was shared across the category. The dimension of latent codes α_i and β, hidden features, and intermediate features were all set to 128. Inspired by [21], ω_s, ω_φ, ω_n, and ω_{Eik} were set to $3e3$, $5e2$, $1e2$, $5e1$ in the $\mathcal{L}_{sdf}$, respectively. In $\mathcal{L}_{reg}$, ω_{intra} and ω_{inter} were set to $1e6$ and $1e2$, respectively. $5e4$ is used in $\mathcal{L}_{cor}$. 4K surface points along with 4K free points were randomly sampled in each iteration. The total epoch was set to 500, and the DGCI model is optimized using an Adam optimizer with a learning rate of $1e-4$ and a batchsize of 16. The experiments were executed on a Linux workstation (Intel Xeon Gold 5119T CPU @ 1.90GHz, 2 NVIDIA Geforce RTX 3090 GPUs). During inference, our method only needs about 10 seconds for one case, revealing that the computational complexity is not heavy.

Evaluation Metrics. To measure the performance of the shape modeling, we adopted the non-manifold(NM) vertices (NM-V), NM edges (NM-E), and NM

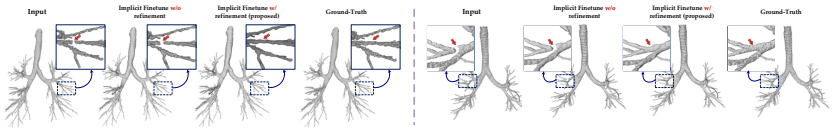

Fig. 6. Visualization of the breakage repair performance by different fine-tune methods. The breakage areas are amplified within the blue boxes for better comparison.

faces (NM-F). NM-V is a vertex connected to three or more non-coplanar faces. NM-E is an edge shared by three or more faces. NM-F refers to faces arranged in such a way that a closed and continuous body cannot be formed. Fewer non-manifold properties indicate better connectivity and smoothness of reconstructed shapes. Tree length detected rate (TD, %), branch detected rate (BD, %), and Dice were used to measure the topological completeness and correctness in the voxel space. Chamfer Distance (CD, mm) and Earth Mover's Distance (EMD, mm) were chosen to measure the performance of the extracted skeleton.

Analysis of the Implicit Shape Modeling Results. To evaluate the shape representation ability on the airway structures of the proposed DGCI, we compared the other state-of-the-art shape modeling methods using implicit representations: Occ Net [15], Conv-Occ Net [17], DeepSDF [16], and DIFNet [5]. Table.1 shows the shape representation accuracy on airway structures, The proposed DGCI achieved the best performance on both the continuous space and the discrete space. Specifically, DGCI can reduce the number of NM-V, NM-E, and NM-F from 30.9, 120.1,and 2102.4 generated by Marching Cube (MC) to 0.0, 4.6, and 253.3. Meanwhile, the reconstructed shapes can achieve 98.6% TD, 99.7% BD, and 91.2% Dice, which proved that DGCI kept the topological structures during the shape modeling. Although the MC with Laplacian smooth could reduce the NM-V and NM-F, however, the number of NM-E had increased. Other implicit methods can consistently reduce the NM-V, NM-E, and NM-F compared to MC. However, they cannot guarantee the connectedness of the reconstructed airway shapes, consequently, their TD and BD are significantly lower than the proposed DGCI. The DGCI can exceed more than 8% TD and BD than other comparative implicit methods, which enhances the clinical value of preoperative surgical path planning. Fig.4 visually demonstrates the superiority of the DGCI in preserving airway structures with high fidelity. More visualization can be found in the Supplementary Material.

Analysis of the Downstream Application Results. For the skeletonization, Table.2 and Fig.5 revealed that cldice [20] and gbo-skel [14] cannot satisfactorily extract the skeleton from complex airway structures. However, our proposed method reduced spike-wise noises existed in the raw annotation of airways, contributing to the improvement of the skeletonization. Table.2 demonstrated that the DGCI can reduce the average CD and EMD from 2.26 and 7.54 to 0.14 and 4.81. Fig.5 corroborated this improvement, as seen in the local details pointed out by yellow arrows, the false positive branches were substantially reduced, which is critical to ensure the accuracy of preoperative surgical path planning. As for the

breakage repair, directly fine-tune the pretrained implicit network would overfit the fractured patterns, as shown in Fig.6. However, equipped with the data refinement before the implicit fine-tune could solve this problem, the breakage parts were repaired by the learned shape prior of the implicit representation.

4 Conclusion

In this paper, we propose a Deep Geometric Correspondence Implicit (DGCI) network to implicitly model the pulmonary airway tree structures in the continuous space. The intrinsic topological regularization shared within the category was explored by a reversible deep correspondence flow on top of the implicit network design. The implicit geometric regularization was further utilized to favor smooth and high-fidelity implicit representation on fine-scaled structures. Compared with the previous works, detailed evaluation results verified the superiority of the DGCI in scalable delineation of airways and downstream applications.

Acknowledgments. This work was supported in part by National Key R&D Program of China (Grant Number: 2022ZD0212400), Natural Science Foundation of China (Grant Number: 62373243) and the Science and Technology Commission of Shanghai Municipality, China (Grant Number: 20DZ2220400), Shanghai Municipal Science and Technology Major Project (No.2021SHZDZX0102).

Disclosure of Interests. The authors have no competing interests to declare that are relevant to the content of this article.

References

1. Attali, D., Boissonnat, J.D., Edelsbrunner, H.: Stability and computation of medial axes-a state-of-the-art report. Mathematical foundations of scientific visualization, computer graphics, and massive data exploration pp. 109–125 (2009)
2. Charbonnier, J.P., Van Rikxoort, E.M., Setio, A.A., Schaefer-Prokop, C.M., van Ginneken, B., Ciompi, F.: Improving airway segmentation in computed tomography using leak detection with convolutional networks. Medical image analysis **36**, 52–60 (2017)
3. Cornea, N.D., Silver, D., Min, P.: Curve-skeleton properties, applications, and algorithms. IEEE Transactions on visualization and computer graphics **13**(3), 530 (2007)
4. David, H., Andrew, M.D., Quoc, V.L.: Hypernetworks. In: Proceedings of International Conference on Learning Representations (2017)
5. Deng, Y., Yang, J., Tong, X.: Deformed implicit field: Modeling 3d shapes with learned dense correspondence. In: Proceedings of the IEEE/CVF Conference on Computer Vision and Pattern Recognition. pp. 10286–10296 (2021)
6. Field, D.A.: Laplacian smoothing and delaunay triangulations. Communications in applied numerical methods **4**(6), 709–712 (1988)

7. Garcia-Uceda Juarez, A., Selvan, R., Saghir, Z., de Bruijne, M.: A joint 3d unet-graph neural network-based method for airway segmentation from chest cts. In: Machine Learning in Medical Imaging: 10th International Workshop, MLMI 2019, Held in Conjunction with MICCAI 2019, Shenzhen, China, October 13, 2019, Proceedings 10. pp. 583–591. Springer (2019)
8. Gropp, A., Yariv, L., Haim, N., Atzmon, M., Lipman, Y.: Implicit geometric regularization for learning shapes. In: International Conference on Machine Learning. pp. 3789–3799. PMLR (2020)
9. Jin, D., Xu, Z., Harrison, A.P., George, K., Mollura, D.J.: 3d convolutional neural networks with graph refinement for airway segmentation using incomplete data labels. In: Machine Learning in Medical Imaging: 8th International Workshop, MLMI 2017, Held in Conjunction with MICCAI 2017, Quebec City, QC, Canada, September 10, 2017, Proceedings 8. pp. 141–149. Springer (2017)
10. Lee, T.C., Kashyap, R.L., Chu, C.N.: Building skeleton models via 3-d medial surface axis thinning algorithms. CVGIP: Graphical Models and Image Processing **56**(6), 462–478 (1994)
11. Lorensen, W.E., Cline, H.E.: Marching cubes: A high resolution 3d surface construction algorithm. In: Seminal graphics: pioneering efforts that shaped the field, pp. 347–353 (1998)
12. Luo, F., Darwiche, K., Singh, S., Torrego, A., Steinfort, D.P., Gasparini, S., Liu, D., Zhang, W., Fernandez-Bussy, S., Herth, F.J., et al.: Performing bronchoscopy in times of the covid-19 pandemic: practice statement from an international expert panel. Respiration **99**(5), 417–422 (2020)
13. Meng, Q., Roth, H.R., Kitasaka, T., Oda, M., Ueno, J., Mori, K.: Tracking and segmentation of the airways in chest ct using a fully convolutional network. In: Medical Image Computing and Computer-Assisted Intervention- MICCAI 2017: 20th International Conference, Quebec City, QC, Canada, September 11-13, 2017, Proceedings, Part II 20. pp. 198–207. Springer (2017)
14. Menten, M.J., Paetzold, J.C., Zimmer, V.A., Shit, S., Ezhov, I., Holland, R., Probst, M., Schnabel, J.A., Rueckert, D.: A skeletonization algorithm for gradient-based optimization. In: Proceedings of the IEEE/CVF International Conference on Computer Vision. pp. 21394–21403 (2023)
15. Mescheder, L., Oechsle, M., Niemeyer, M., Nowozin, S., Geiger, A.: Occupancy networks: Learning 3d reconstruction in function space. In: Proceedings of the IEEE/CVF conference on computer vision and pattern recognition. pp. 4460–4470 (2019)
16. Park, J.J., Florence, P., Straub, J., Newcombe, R., Lovegrove, S.: Deepsdf: Learning continuous signed distance functions for shape representation. In: Proceedings of the IEEE/CVF conference on computer vision and pattern recognition. pp. 165–174 (2019)
17. Peng, S., Niemeyer, M., Mescheder, L., Pollefeys, M., Geiger, A.: Convolutional occupancy networks. In: Computer Vision–ECCV 2020: 16th European Conference, Glasgow, UK, August 23–28, 2020, Proceedings, Part III 16. pp. 523–540. Springer (2020)
18. Qin, Y., Zheng, H., Gu, Y., Huang, X., Yang, J., Wang, L., Yao, F., Zhu, Y.M., Yang, G.Z.: Learning tubule-sensitive cnns for pulmonary airway and artery-vein segmentation in ct. IEEE transactions on medical imaging **40**(6), 1603–1617 (2021)
19. Reynisson, P.J., Leira, H.O., Hernes, T.N., Hofstad, E.F., Scali, M., Sorger, H., Amundsen, T., Lindseth, F., Langø, T.: Navigated bronchoscopy: a technical review. Journal of bronchology & interventional pulmonology **21**(3), 242–264 (2014)

20. Shit, S., Paetzold, J.C., Sekuboyina, A., Ezhov, I., Unger, A., Zhylka, A., Pluim, J.P., Bauer, U., Menze, B.H.: cldice-a novel topology-preserving loss function for tubular structure segmentation. In: Proceedings of the IEEE/CVF Conference on Computer Vision and Pattern Recognition. pp. 16560–16569 (2021)
21. Sitzmann, V., Martel, J., Bergman, A., Lindell, D., Wetzstein, G.: Implicit neural representations with periodic activation functions. Advances in neural information processing systems **33**, 7462–7473 (2020)
22. Wan, I.Y., Toma, T.P., Geddes, D.M., Snell, G., Williams, T., Venuta, F., Yim, A.P.: Bronchoscopic lung volume reduction for end-stage emphysema: report on the first 98 patients. Chest **129**(3), 518–526 (2006)
23. Yu, X., Rao, Y., Wang, Z., Liu, Z., Lu, J., Zhou, J.: Pointr: Diverse point cloud completion with geometry-aware transformers. In: Proceedings of the IEEE/CVF international conference on computer vision. pp. 12498–12507 (2021)
24. Zhang, M., Gu, Y.: Towards connectivity-aware pulmonary airway segmentation. IEEE Journal of Biomedical and Health Informatics (2023)
25. Zhang, M., Wu, Y., Zhang, H., Qin, Y., Zheng, H., Tang, W., Arnold, C., Pei, C., Yu, P., Nan, Y., et al.: Multi-site, multi-domain airway tree modeling. Medical Image Analysis **90**, 102957 (2023)
26. Zhao, M., Zhao, S., Quan, Q., Fan, L., Qiu, X., Liu, S., Zhou, S.K.: Gdds: Pulmonary bronchioles segmentation with group deep dense supervision. arXiv preprint arXiv:2303.09212 (2023)
27. Zhao, T., Yin, Z., Wang, J., Gao, D., Chen, Y., Mao, Y.: Bronchus segmentation and classification by neural networks and linear programming. In: Medical Image Computing and Computer Assisted Intervention–MICCAI 2019: 22nd International Conference, Shenzhen, China, October 13–17, 2019, Proceedings, Part VI 22. pp. 230–239. Springer (2019)
28. Zheng, H., Qin, Y., Gu, Y., Xie, F., Yang, J., Sun, J., Yang, G.Z.: Alleviating class-wise gradient imbalance for pulmonary airway segmentation. IEEE transactions on medical imaging **40**(9), 2452–2462 (2021)